iScience

CellPress
OPEN ACCESS

Article

Deep mineralization of VOCs in an embedded hybrid structure $CoFe_2O_4/MoS_2$/PMS wet scrubber system

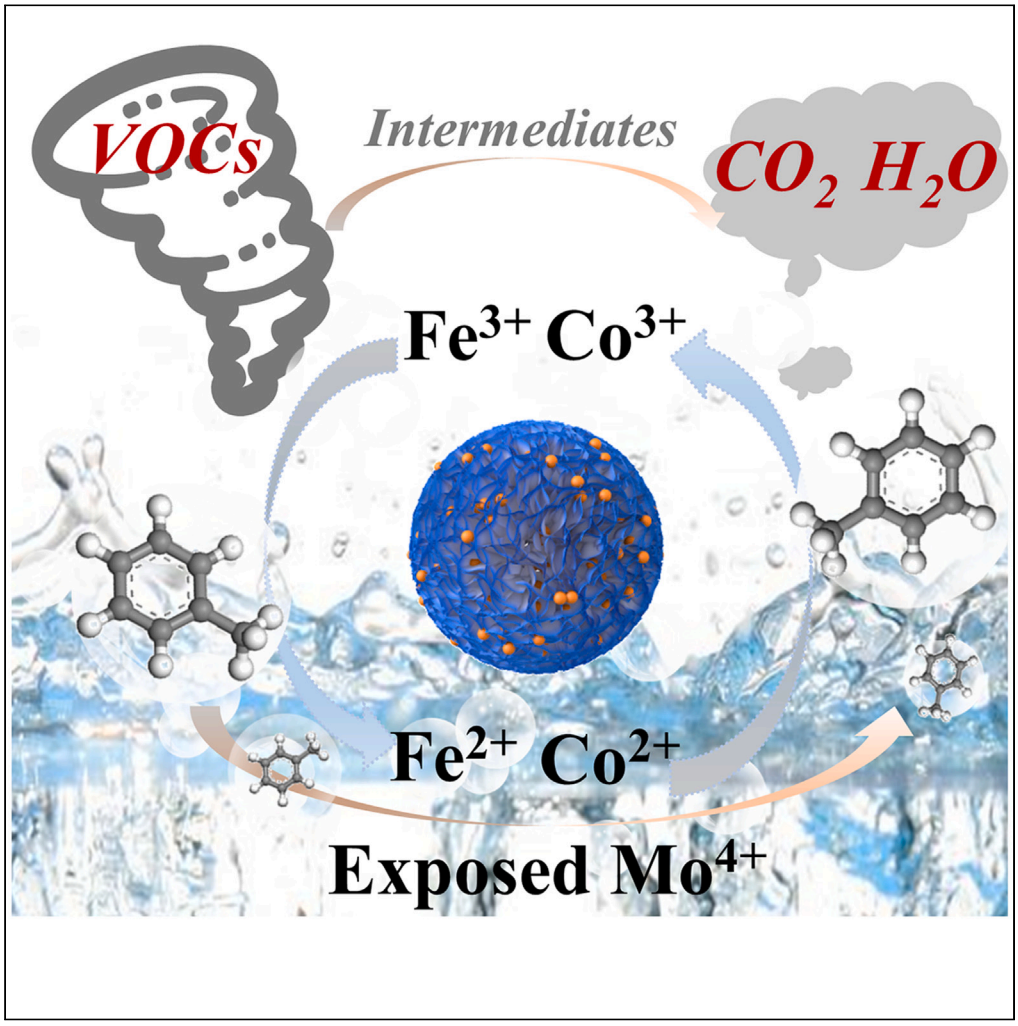

Xiai Zhang, Wenquan Zhang, Xinwei Zhang, ..., Hao Zhu, Zhimao Yang, Chuncai Kong

kongcc@xjtu.edu.cn

Highlights

The $CoFe_2O_4/MoS_2$/PMS system can effectively degrade gaseous toluene

The catechol structural surfactant was introduced to synthesize $CoFe_2O_4$ nanospheres

The $CoFe_2O_4/MoS_2$ composite catalyst has excellent catalytic stability

The MoS_2 offers ample reduction sites for facilitating PMS activation

Zhang et al., iScience 26, 108054
October 20, 2023
https://doi.org/10.1016/j.isci.2023.108054

iScience

CellPress
OPEN ACCESS

Article

Deep mineralization of VOCs in an embedded hybrid structure $CoFe_2O_4/MoS_2$/PMS wet scrubber system

Xiai Zhang,[1,4] Wenquan Zhang,[2,4] Xinwei Zhang,[1] Jun Li,[1] Tong Wang,[1] Qikui Fan,[1] Hao Zhu,[3] Zhimao Yang,[1] and Chuncai Kong[1,5,*]

SUMMARY

Peroxymonosulfate (PMS)-based advanced oxidation processes in liquid phase systems can actively degrade toluene. In this work, the catechol structural surfactant was introduced to synthesize the dispersed and homogeneous $CoFe_2O_4$ nanospheres and embedded into MoS_2 nanoflowers to form magnetically separable heterojunction catalysts. The innovative approach effectively mitigated the traditionally low reduction efficiency of transition metal ions during the heterogeneous activation process. In $CoFe_2O_4/MoS_2$/PMS system, the toluene removal efficiency remained 95% within 2 h. The contribution of $SO_4^{\cdot-}$, $\cdot O_2^-$, $\cdot OH$, and $^1O_2$ was revealed by radical quenching experiment and electron paramagnetic resonance spectroscopy. The results illustrated that MoS_2 offers ample reduction sites for facilitating PMS activation via Fe^{3+}/Fe^{2+} redox interactions. Furthermore, an investigation into the toluene degradation pathway within the $CoFe_2O_4/MoS_2$/PMS system revealed its capability to suppress the formation of toxic byproducts. This ambient-temperature liquid-phase method presented promising route for the removal of industrial volatile organic pollutants.

INTRODUCTION

The term "volatile organic compounds" (VOCs) designates a class of organic compounds characterized by a boiling point range of 50°C–260°C at atmospheric pressure and a saturated vapor pressure exceeding 133.32 Pa at room temperature.[1–3] VOCs are air pollutants that are widely emitted during production processes in the chemical, ceramics, paints, and coatings industries. Furthermore, they constitute a significant portion of total organic content found in petroleum or refinery wastewater, often containing various aromatic hydrocarbons.[4] The emission of VOCs has been increasing serious environmental problems and putting human health at risk, leading to symptoms such as dizziness, headaches, memory impairment, vision impairment, and even fatalities.[5,6] A majority of VOCs encompass alkanes, alkenes, alkynes, aromatics, aldehydes, and sulfur/nitrogen compounds, with aromatics and alkenes particularly being highly detrimental molecules, significantly contributing to haze and photochemical ozone creation.[7–9]

Currently, primary methods for VOCs treatment involve adsorption recovery, photocatalytic decomposition, catalytic combustion method, and biological method.[10–12] The substantial concentration of VOCs and non-biodegradable components renders standalone biological treatment unviable. Despite advancements in mitigating chemical waste gas pollution, challenges like elevated treatment costs, short equipment and catalyst lifespans, extended catalyst regeneration cycles, and potential secondary pollution persist.[13] Researchers have explored various removal methods for monocyclic and polycyclic aromatic hydrocarbons, including UV/oxidant based AOPs, Fenton and photo-Fenton processes, photocatalysis, electrochemical advanced oxidation processes, sulfate radical based advanced oxidation process (AOPs) and other techniques.[14] Additionally, the researchers proposed a hybrid approach based on the combination of cavitation and advanced oxidation to enhance the oxidation capacity. The hybrid process is capable of degrading persistent pollutants and reducing the overall consumption of energy and oxidants.[15] Among these techniques, AOPs has been recognized as a promising means of removing gaseous VOCs via wet bubbling scrubber systems.[16,17] The mechanism hinges on transferring gaseous VOCs to the liquid phase, capitalizing on the robust oxidation capacity of potent reactive oxygen species to comprehensively degrade VOCs into harmless carbon dioxide and water.[16,18,19] The conventional AOPs, hydrogen peroxide (H_2O_2), persulfate (including PS, PMS, and PDS), and ozone (O_3) are activated by the catalyst to produce free

[1]Ministry of Education Key Laboratory for Non-equilibrium Synthesis and Modulation of Condensed Matter, Shaanxi Province Key Laboratory of Advanced Functional Materials and Mesoscopic Physics, School of Physics, Xi'an Jiaotong University, Xi'an 710049, P.R. China
[2]Shaanxi Coal and Chemical Industry Technology Development Center Co., Ltd., Xi'an 710100, Shaanxi, P.R. China
[3]Key Laboratory of Western China's Environmental Systems (Ministry of Education) and Gansu Engineering Research Center of Fine Particles Pollution Control Technology and Equipment, College of Earth and Environmental Sciences, Lanzhou University, Lanzhou 730000, P.R. China
[4]These authors contributed equally
[5]Lead contact
*Correspondence: kongcc@xjtu.edu.cn
https://doi.org/10.1016/j.isci.2023.108054

radicals [such as hydroxyl (·OH), sulfate ($SO_4^{\bullet-}$), and superoxide ion radicals ($O_2^{\bullet-}$)].[20–22] While ·OH has been the main reactive radical in traditional AOPs for pollutant degradation, sulfate radical-based AOPs ($SO_4^{\bullet-}$-AOPs) typically utilize PMS as a precursor for producing $SO_4^{\bullet-}$ via peroxide bond cleavage in the PMS molecule through energy and electron transfer reactions.[23] Notably, sulfate radical exhibit higher redox potential (E_0 ($SO_4^{\bullet-}$) = 2.5–3.1 eV), longer half-life, and wider pH range than hydroxyl radical in the removal of benzene series VOCs.[24,25] Thus, sulfate radical offers more efficient decomposition and mineralization ability in the removal of VOCs.

$SO_4^{\bullet-}$ is generally generated by ultraviolet/visible light irradiation, heating, or the activation of persulfates with carbon or transition metal catalysts.[26–28] Compared with photocatalysis/thermal catalysis, transition metal catalysis for PMS activation has been favorable, as devoid of external energy.[29–32] Transition metals like Co, Fe, Cu, and Mn offer low cost-effectiveness and reusability, allowing for effective catalytic oxidation of PMS. For instance, Yuan et al.[33] synthesized three-dimensional mesoporous α-$Co(OH)_2$ nanosheets on nickel foam (NF) by a facile electrodeposition method, and the $Co(OH)_2$/NF-activated PMS could almost completely remove phenol at 7 min, which had outstanding catalytic performance. Bimetallic catalysts with a spinel structure possessing special geometric and electronic structures can exhibit high stability, with $CoFe_2O_4$, a prominent ferrite, showcasing outstanding catalysis, magnetic recovery, and stability. However, the slow regeneration rate of Co^{3+} and Fe^{3+} catalytic sites in cobalt ferrite limits its practical application. In this context, synergistic coupling and enhanced conductivity between spinel ferrite and active substances substantially enhance catalytic performance.[34] Molybdenum sulfide, resembling graphite in its two-dimensional layered structure, offers abundant active sites and high electron mobility.[35] It can be used as a co-catalyst to accelerate the cycle of Fe^{3+}/Fe^{2+}.[36] The abundance of unsaturated sulfur atoms on MoS_2 surface captures protons and exposes Mo^{4+} reducing metal ions, facilitating catalyst reactivation and enhancing oxidant decomposition.[37] A single reduction pathway based on metal ions is not sufficient for efficient degradation. Therefore, the design of complex catalysts with unique structures can provide more reducing charges for active centers regeneration.

Herein, homogeneous cobalt ferrite nanospheres were successfully prepared by introducing small molecule compounds with short-chain structure. The nanospheres were embedded into molybdenum sulfide nanoflowers through a one-step hydrothermal method, resulting in catalysts with a unique hybrid structure. The typical VOC, toluene was selected to investigated the catalytic potential of the $CoFe_2O_4$/MoS_2/PMS system for toluene removal. We systematically evaluated the effect of catalyst dosage, PMS concentration, initial pH, and inhibitors on toluene decomposition efficiency. The $CoFe_2O_4$/MoS_2/PMS system achieved efficient and consistent oxidation performance than $CoFe_2O_4$/PMS system. Free radical species were identified using electron paramagnetic resonance spectroscopy (EPR), and their contribution to the degradation process was further analyzed through radical quenching experiments. Combining experimental data with theoretical calculations, it was proved that the protonation on the surface of MoS_2 induces sulfur vacancy, which led to the highly exposed Mo^{4+} site and enhanced Fe^{3+}/Fe^{2+} cycle. The embedded hybrid $CoFe_2O_4$/MoS_2 activated PMS system facilitated extensive toluene mineralization, rendering it highly promising for industrial applications.

RESULTS AND DISCUSSION

Characterization of the catalysts

Figure 1 depicted the schematic representation of CF/MS embedded hybrid structure. The morphology and composition of the obtained products were extensively examined by TEM, FESEM, and EDX mapping. As shown in Figures 1C1 and 1C2, cobalt ferrite nanospheres were uniformly embedded into molybdenum sulfide nanoflowers, forming composite catalyst with embedded hybrid structure. The magnetic cobalt ferrites regulated by the short-chain surfactant dopamine showed highly dispersed, uniform, and spheroidal morphology with an average particle size of 200 nm (Figures 1A1 and 1A2). The measured lattice spacing was 0.254 nm, 0.27 nm, and 0.62 nm, corresponding to the crystal planes of CF (311) and MS ((100) and (002)), respectively.[38,39] From an economic and environment-friendly perspective, dopamine (DA) as a surfactant and interparticle linker was employed instead of traditional surfactants.[40,41] DA as bidentate enediol ligands facilitated strong coordination affinity to magnetite surface sites, binding the catechol groups originating from DA molecules on the magnetite nanocrystal cluster surfaces, thus forestalling aggregation into sizable single crystals.[42] The TEM and SEM-EDS elemental mapping indicated the high dispersions of Co, Fe, O, Mo, and S elements within CF and CF/MS (Figures 1E–1I).

The X-ray diffraction analysis confirmed the formation of the crystal structure. As shown in Figure 2A, the well-defined diffraction peaks were observed at 18.24°, 30.06°, 35.45°, 37.28°, 43.47°, 53.89°, 57.17°, and 62.73°, aligning with crystal planes (111), (220), (311), (222), (400), (422), (511), and (440) (JCPD#03–0864). The diffraction peaks at 32.6°, 36.4°, and 58.2° align convincingly with the standard pattern of 2H-MoS_2 phase (JCPDS no. 37–1492). Additionally, two distinct peaks at 9.36° and 18.7° belong to crystal planes (002) and (004) of 1T-MoS_2.[43] FTIR analysis of the different catalysts was studied as shown in Figure 2B. The strong transmission bands appeared at 585 cm^{-1}, which could be attributed to the tensile vibration mode of spinel CF nanospheres. The presence of an S-S bond at 821-985 cm^{-1} and a Mo-S bond at 608 cm^{-1} became evident in MS. Furthermore, a hydroxyl peak at 3427 cm^{-1} was observed in all catalysts, verifying the existence of the surface hydroxyl groups. The characteristic peaks of the FTIR spectra were consistent with XRD analysis, confirming the successful synthesis of the target product. As shown in Figure 2C, the catalyst could be easily separated from the solution under the action of an external magnetic field. The VSM characterization revealed that the catalyst has good ferromagnetism, which had a saturation magnetization intensity of 0.5 emu/g and it was easy to separate and collect during practical application.

For in-depth analysis, X-ray photoelectron spectroscopy (XPS) was carried out to explore the elemental composition and valence states of CF, MS and CF/MS. The full-scan spectrum showed the presence of Co, Fe, O, Mo, and S in the sample (Figure 3A). The fine spectrum fitting of Co 2p for $CoFe_2O_4$ exhibited that the peaks with binding energies at 795.87 eV and 779.89 eV correspond to Co^{2+} $2p_{1/2}$ and Co^{2+} $2p_{3/2}$, respectively. Notably, the peak at 782.05 eV was ascribed to Co^{3+} $2p_{3/2}$ within the octahedral site. Of note, the peaks at 802.94 eV and 786.38 eV were satellite peaks. Similarly, the two peaks with binding energies at 713.17 eV and 724.87 eV correspond to Fe^{3+} $2p_{3/2}$ and

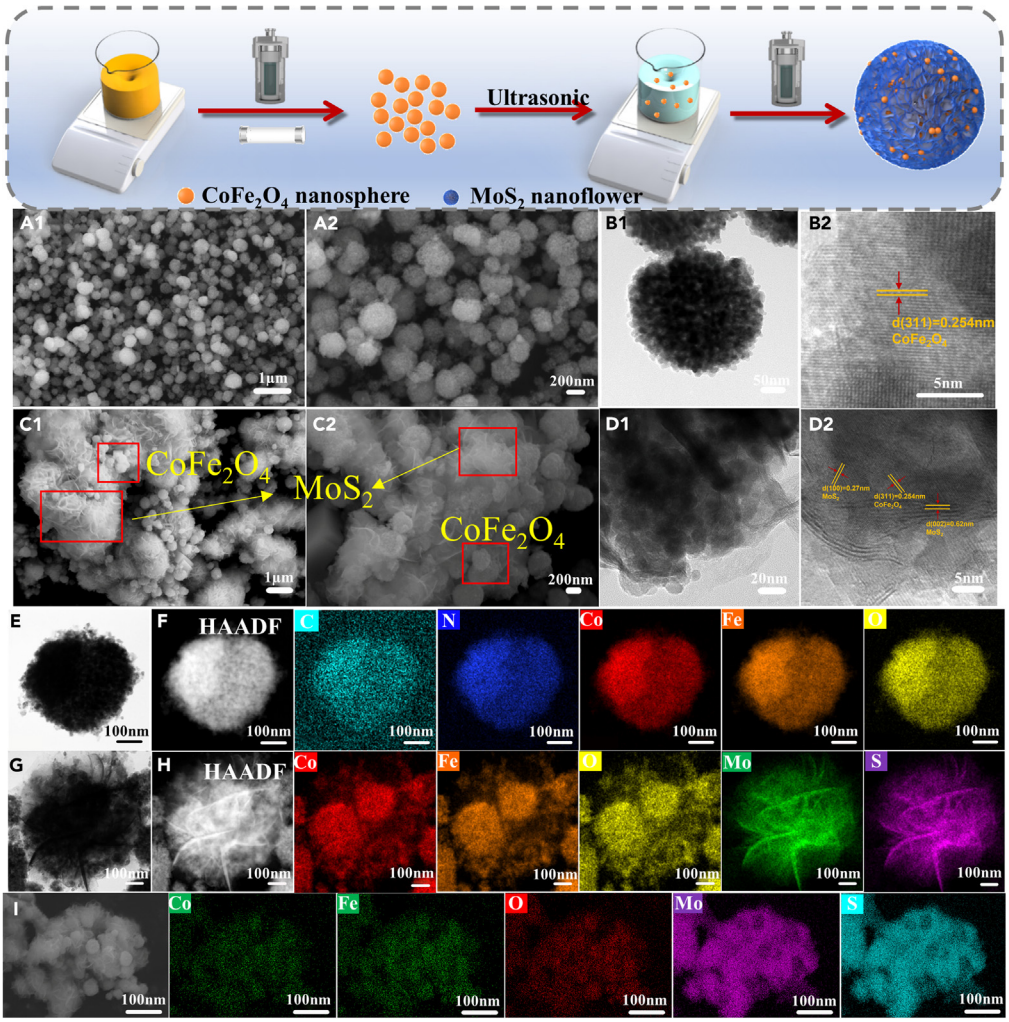

Figure 1. Schematic diagram of catalyst preparation and morphology characterization

(A1 and A2) SEM images of CF.

(B1 and B2) TEM images and HRTEM images of CF.

(C1 and C2) SEM images of CF/MS.

(D1 and D2) TEM images and HRTEM images of CF/MS.

(E–H) TEM elemental mapping images of CF and CF/MS.

(I) SEM-EDS elemental mapping images of CF/MS.

Fe^{3+} $2p_{1/2}$, respectively. The peak at 710.59 eV was attributed to Fe^{2+} $2p_{3/2}$. The peaks at 732.79 eV and 718.51 eV were satellite peaks. It was worth noting that the combination with MoS_2 enables the peak positions of Fe 2p, Co 2p, and O 1s toward the high binding energy, which is due to the introduction of more electronegative Mo, resulting in redox reaction during the binding of $CoFe_2O_4$ and MoS_2.[44,45] The conjecture was further validated in the Mo 3d and S 2p spectra. As depicted in the Figure 3E, after compounding with MoS_2, the relative content of Mo^{5+} (229.81 eV) and Mo^{6+} (232.52 eV, 235.86 eV) on the surface of composite catalyst increases significantly, and the peak position of Mo^{4+} shifts from 229.33 eV to low binding energy (228.83 eV). The $2p_{1/2}$ and $2p_{3/2}$ peaks of S in MoS_2 were located at 163.48 eV and 162.32 eV, respectively. The characteristic peak (edge S) strengths at 164.77 eV of CF/MS increased compared with MoS_2, further indicating the formation of Mo-S-Fe and Mo-S-Co bonds at the junction of MoS_2 and $CoFe_2O_4$.[46] Moreover, the O 1s peak at 530.30 eV of $CoFe_2O_4$ was a typical metal-oxygen bond (Fe-O/Co-O), the peak at 531.63 eV was associated with adsorbed oxygen. The O 1s XPS peak location shifts toward a high binding energy after being combined with MoS_2.

Toluene degradation performance

Figure 4 illustrated the quantitative analysis of toluene degradation facilitated by the prepared catalysts. As delineated in Figure S6, in the presence of PMS alone, the initial toluene removal was attributed to water absorption, the removal efficiency decreased rapidly with time, while the

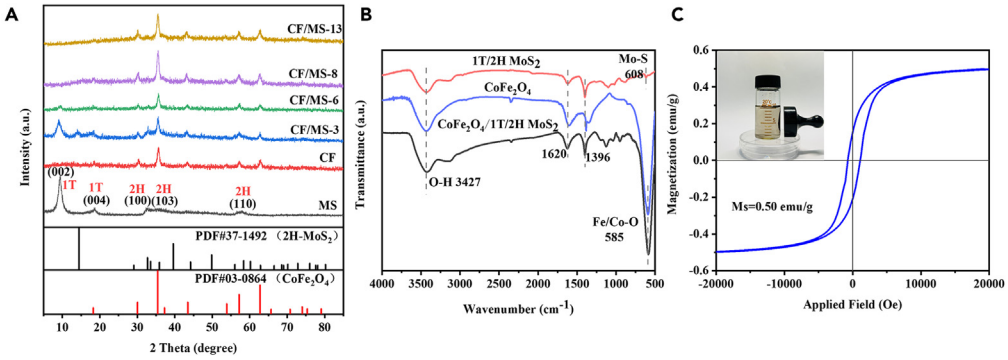

Figure 2. Structural characterization of catalysts

(A) XRD patterns of catalysts.

(B) FT-IR spectra of MS, CF, and CF/MS.

(C) VSM characterization and magnetic diagram of CF/MS.

carbon dioxide production tended to zero also verified this result, and the experiment proved that the PMS system could not degrade toluene effectively. The toluene conversion efficiencies of MoS_2 and $CoFe_2O_4$-activated PMS were 34.7% and 81.3%, respectively, and the removal efficiency gradually decreased with the extension of degradation time. In the CF/MS/PMS system, a substantial and stable removal efficiency was observed when compared to MS/PMS and CF/PMS systems. The degradation efficiencies of CF/MS-3, CF/MS-6, CF/MS-8, CF/MS-13 were measured at 73.22%, 94.43%, 94.82%, and 96.82%, respectively. Research into the effect of initial PMS concentration revealed that a molar ratio of the oxidant to toluene equal to 0.003 was favorable for efficient toluene degradation. It was indicated that the remarkable catalytic performance was attributed to the synergistic catalysis of CF and MS. The addition of MoS_2 as co-catalyst could significantly enhance the conversion of Fe^{3+} to Fe^{2+}, and further boosted the efficiency of toluene degradation.[45] Turning to an essential indicator measuring the extent of toluene

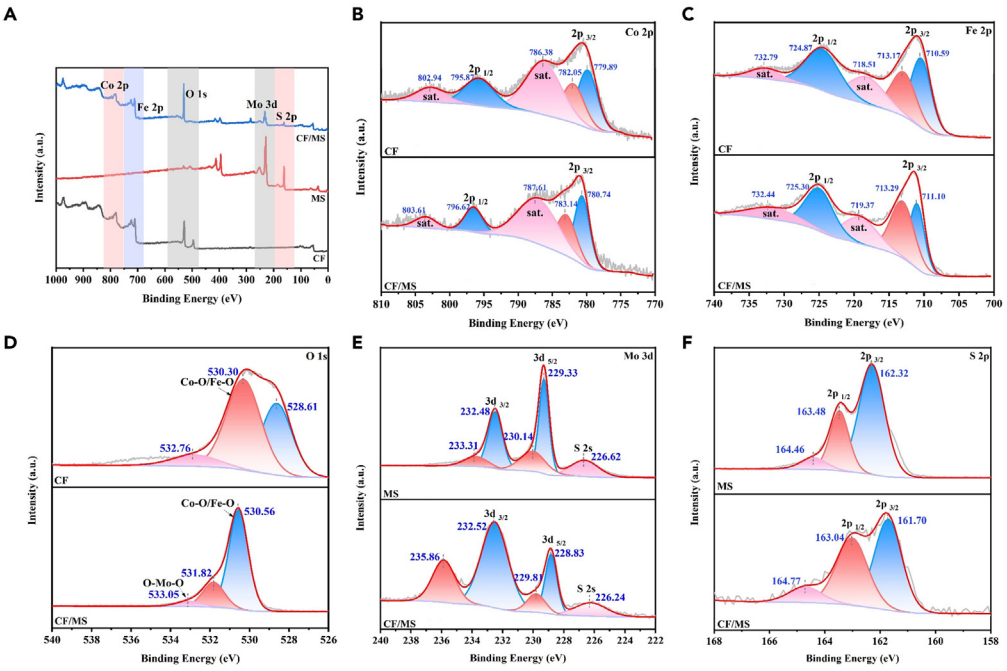

Figure 3. XPS spectra of CF, MS, and CF/MS

(A) Survey.

(B) Co 2p.

(C) Fe 2p.

(D) O 1s.

(E) Mo 3days.

(F) S 2p.

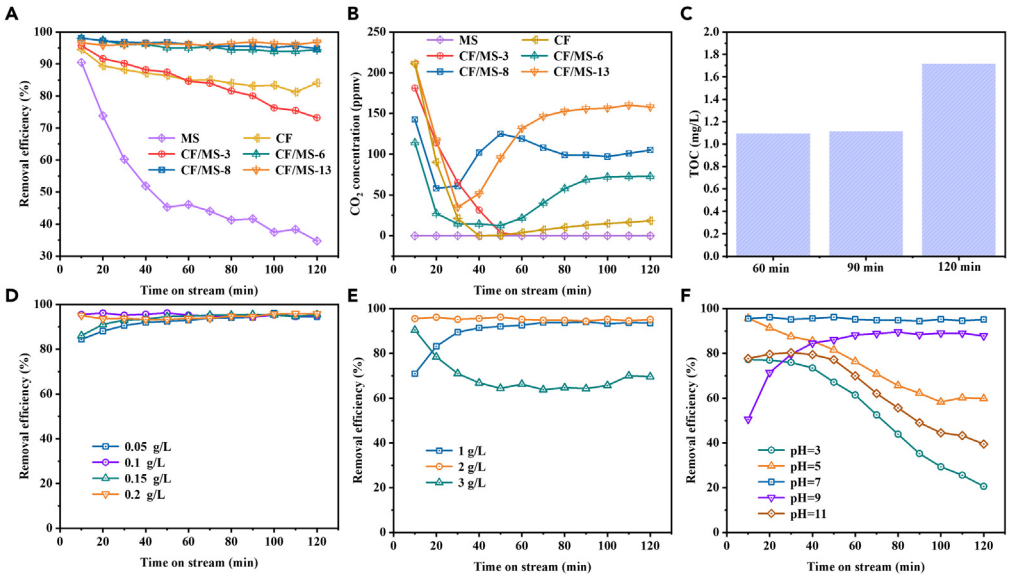

Figure 4. Influence of reaction systems on the degradation of toluene

(A and B) Removal efficiency and CO_2 concentration of different materials.

(C) TOC concentration with time in solution of CF/MS/PMS system.

(D) Effect of catalyst dosage.

(E) Effect of PMS concentration.

(F) Effect of initial pH for toluene degradation. ([Toluene] = 30 ppm; [catalyst dosages] = 0.1 g/L; [PMS concentration] = 2 g/L; T = 30°C; $[pH]_0$ = 7).

mineralization, the CO_2 outlet concentration produced by different catalysts was detected in the tail gas (Figure 4B). The MS/PMS reaction system demonstrated minimal CO_2 generation. The molar concentration of CO_2 produced by CF/PMS stabilizes at 18 ppm. Notably, CF/MS/PMS composite system revealed excellent performance in toluene mineralization process. The CO_2 produced by CF/MS-3, CF/MS-6, CF/MS-8, and CF/MS-13 activated PMS is 395.74 ppm, 589.01 ppm, 1216.45 ppm, and 1571.14 ppm, respectively. TOC concentration was further analyzed in the aqueous solution of CF/MS/PMS systems with time (Figure 4C). The liquid samples were collected at intervals of 60 min, 90 min, and 120 min during the course of catalytic reaction for TOC analysis. The TOC values exhibited an upward trend, which indicated intermediates accumulated in the water. The result further confirmed the excellent mineralization ability of the composite catalytic system.

The effect of different catalyst dosages on toluene degradation was evaluated in CF/MS/PMS system. From Figure 4D, at catalyst dosages of 0.05 g/L, 0.1 g/L, 0.15 g/L, and 0.2 g/L, the toluene removal rates remained consistently above 95%, exhibiting no obvious attenuation trend within 120 min. In addition, a comparative exploration of PMS addition was conducted (Figure 4E). The degradation rate was obviously slow within the initial 30 min at a PMS dosage of 1 g/L. Upon raising the PMS concentration to 3 g/L, a decrease in degradation efficiency was observed. This phenomenon could be attributed to two primary factors. On the one hand, excessive PMS addition might inhibit the consumption of the generated $SO_4^{\bullet-}$, thus hindering the catalytic reaction and potentially transforming them into weaker oxidant species, such as $SO_5^{\bullet-}$. On the other hand, the presence of abundant PMS in the solution could influence the pH balance by generating protons. This disturbance in the pH environment due to elevated PMS levels could lead to suppressed catalyst activity and consequently result in a deceleration of the degradation efficiency.[24] This phenomenon had been extensively investigated and could be better understood through the pH dependency study (Figure 4F). As illustrated in Figure 4F, highly acidic and strongly alkaline conditions noticeably diminished the removal efficiency of toluene, with conversion rates sharply dropping to 20.63% when the pH reached 3. Under mildly acidic conditions (pH = 5), the initial 10 min degradation efficiency was 95.74%, which subsequently decreased to 60% after 2 h. This phenomenon could be attributed to the detrimental impact of excess H^+ ions, disrupting the initial catalyst complexation and occupying active sites, thereby inhibiting the adsorption and further activation of PMS. Simultaneously, the presence of an excessive quantity of chloride anions in the solution, due to the excessive consumption via reaction with hydroxyl radicals, hindered the oxidation of pollutants upon the evident addition of hydrochloric acid, consequently diminishing the degradation efficiency of the target pollutants.[47] Under mildly alkaline conditions (pH = 9), the initial 10 min removal efficiency was relatively low (50.61%), gradually increasing thereafter. However, as the pH rises to 11, the conversion rate of toluene declined to 39.53%. On one hand, the surplus OH^- ions transformed HSO_5^- into SO_5^{2-}, with limited capability for SO_5^{2-} to further convert into $SO_4^{\bullet-}$. Additionally, the strong alkaline conditions accelerated the transformation of $SO_4^{\bullet-}$ into ·OH, which was unfavorable for toluene conversion. On the other hand, in high pH environments, the protonated H^+ ions could capture unsaturated S atoms on the catalyst surface, generating H_2S and thus rendering the active sites of Mo^{4+} inaccessible.

In practical engineering applications, co-existing inorganic anions in wastewater could exert adverse effects on the removal of target pollutants. Hence, a thorough evaluation of the impacts of Cl^-, HCO_3^-, NO_3^-, and $H_2PO_4^-$ on toluene removal efficiency was specifically

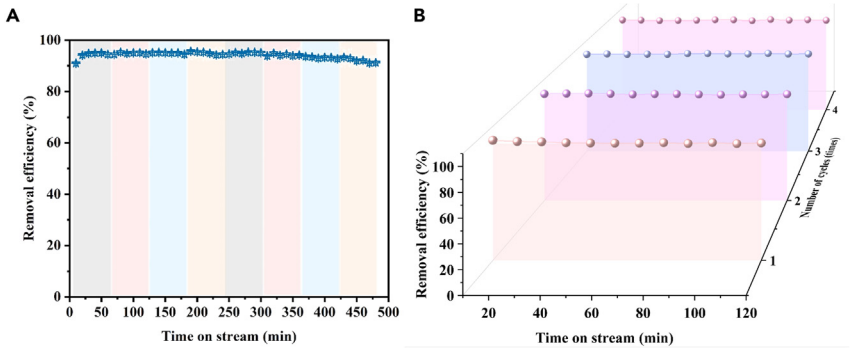

Figure 5. Cyclic stability of catalysts

(A) Degradation efficiency of toluene by continuous 8 h reaction ([Toluene] = 30 ppm; [catalyst dosages] = 0.1 g/L; [PMS concentration] = 2 g/L; T = 30°C; $[pH]_0$ = 7).

(B) Cycle efficiency in four consecutive cycles by re-adding PMS ([re-adding PMS concentration] = 1 g/L).

conducted. As illustrated in Figure S7, Cl^- and HCO_3^- exhibited inhibitory effects on toluene degradation at rates of 30.91% and 13.22%, respectively. Within the initial 30 min, NO_3^- demonstrated a suppressive effect of 9.27% on toluene degradation, with an overall effect that could be considered negligible. The decreased degradation efficiency with HCO_3^- was also observed because the scavenging effect and the low reactivity of the resulting secondary species toward the pollutant and vice versa.[48] Free radical quenching experiments and EPR characterization also confirmed that $SO_4^{\bullet-}$ play a dominant role in the degradation process. Intriguingly, HPO_4^{2-} displayed the most pronounced impact, with toluene removal efficiency is almost zero after 2 h, indicating almost complete inhibition by the presence of HPO_4^{2-}. The research indicated that phosphates possessed a substantial affinity for the surface of ferrite oxides, forming complexes with surface-bound Fe^{3+}. It could be inferred that this interaction was related to the substitution of active sites such as surface hydroxyl groups, influencing the catalytic capability of the catalyst through their substitution.[49] The demonstrated results underscored the significance of understanding the intricate interactions between inorganic anions and catalytic surfaces in enhancing pollutant removal efficiency within complex treatment systems. Moreover, it was noteworthy that the formation of nitro-substituted products was quite common in advanced oxidation processes (AOPs) in the presence of nitrite or nitrate ions. Nitro compounds constitute one of the toxic byproducts generated during wastewater treatment processes. Hence, when employing liquid-phase wet scrubbing techniques for the treatment of gaseous VOCs, careful attention must be paid to the potential secondary pollution risk arising from the formation of nitro-substituted compounds due to the presence of nitrate ions in the liquid phase.[50] Furthermore, the selection of inorganic acid species for adjusting the solution pH could also influence the degradation efficiency of pollutants. This phenomenon primarily stems from ion recombination, the generation of novel radical species, or the scavenging of radicals through reactions with inorganic ions, subsequently leading to either enhancement or diminishment in the degradation efficiency of target organic pollutants.[47]

For the practical application of industrial VOCs removal, the continuous stability and cyclic stability of heterogeneous catalysts were very important. Figure 5 represented the stability and cyclic stability of the developed composite catalyst under long-term continuous operation. Employing a fixed quantity of catalyst and PMS, the toluene removal efficiency remained above 90% for continuous 8 h reaction, confirming the excellent continuous stability of the catalyst. Furthermore, after adding fresh PMS every 120 min, the toluene conversion rate was stable above 95% after 4 consecutive cycles, which indicated that the synthesized composite catalyst exhibits good cyclic stability.

PMS activation mechanism

In order to obtain the activation mechanism of PMS in CF/MS/PMS system, the surface element valence states of Co/Fe/O/Mo/S after degradation were determined by XPS analysis. The binding energies at 796.63 eV (796.62 eV) and 782.80 eV (783.14 eV) were assigned to Co^{3+} $2p_{1/2}$ and Co^{3+} $2p_{3/2}$; the binding energies at 796.63 eV (796.62 eV) and 780.44 eV (780.74 eV) were attributed to Co^{2+} $2p_{1/2}$ and Co^{2+} $2p_{3/2}$. Similarly, Fe $2p_{1/2}$ at 725.56 eV (725.30 eV) and Fe $2p_{3/2}$ at 711.38 eV (711.10) were attributed to Fe^{2+}, Fe $2p_{1/2}$ at 725.56 eV (725.30 eV) and Fe $2p_{3/2}$ at 714.18 eV (713.30 eV) belong to Fe^{3+}, respectively. Figure 6 displayed the change in the valence states of elements after the reaction. Fe elements on the surface possess obvious valence change i.e., Fe^{2+} content reduced by 13.8% and Fe^{3+} content increased by 10.6%. Thus, Fe sites on the catalyst surface participate in the activation of PMS. With the progress of catalytic reaction, the ratio of peak area of Co^{2+}/Co^{3+} is nearly unchanged i.e., Co^{2+} was first oxidized to Co^{3+}, and then participated in the formation of $^1O_2$. After the reaction, the binding energy of Mo $3d_{5/2}$ is increased from 228.83 eV (before the reaction, Figure 3E) to 229.39 eV, the binding energy of Mo $3d_{3/2}$ is increased from 232.52 eV (before the reaction, Figure 3E) to 232.68 eV, and the binding energy of S 2s is increased from 226.24 eV (before the reaction, Figure 3F) to 226.99 eV, while binding energy of O 1s is unchanged (Figure 6D). Results revealed that Mo 3days and S 2s orbitals lost electrons, and the excited electrons mainly come from Co 2p and Fe 2p orbitals instead of O 1s orbital. Figure 8 assumed the proposed toluene degradation pathway. In the process of activating PMS, high-state Fe and Mo ions are reduced to low-state, forming a stable redox cycle.[44] In addition, the interaction of $SO_5^{\bullet-}$ with H_2O also accelerates the formation of $^1O_2$.[51] To sum up, the degradation mechanism of toluene in CF/MS/PMS system includes the following four processes. (a) Fe^{2+}/Fe^{3+}, Co^{2+}/Co^{3+} on $CoFe_2O_4$ surface activates PMS to produce $SO_4^{\bullet-}$ free radical

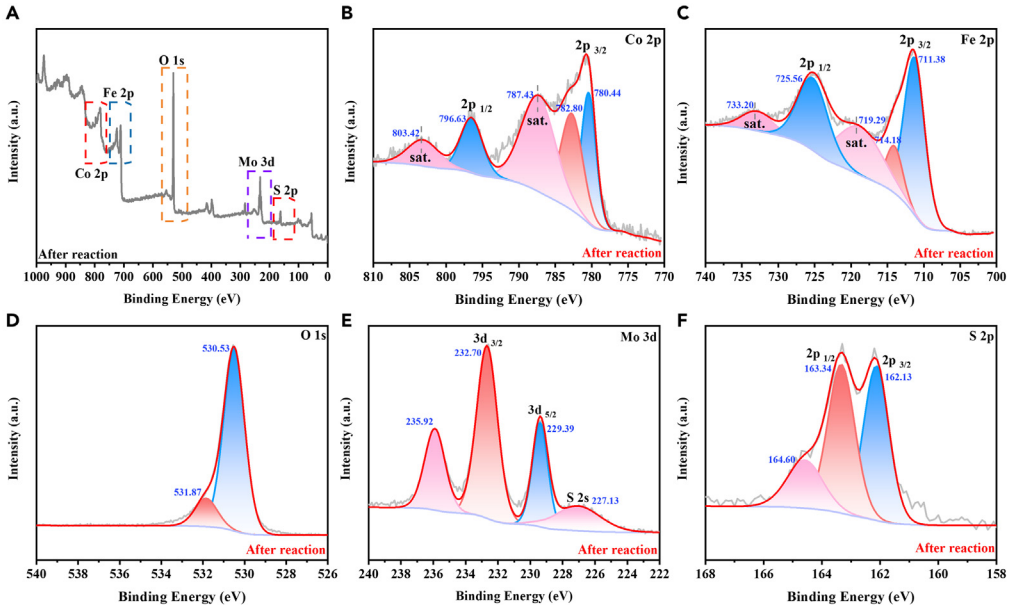

Figure 6. XPS spectra of catalysts after reaction

(A) Survey.

(B) Co 2p.

(C) Fe 2p.

(D) O 1s.

(E) Mo 3days.

(F) S 2p.

(Equations 1–4).[52] (b) the affinity of MoS_2 for intermediates during the activation of MoS_2 in PMS is conducive to accelerating the redox reaction between Fe^{3+} and Fe^{2+} (Equations 5–7).[53] (c) the formation of $^1O_2$ occurs by the interaction between H_2O and $SO_5^{\cdot-}$ (Equation 8). (d) H_2O can combine with $SO_4^{\cdot-}$ to form $O_2^{\cdot-}$, which is further transformed into $^1O_2$ (Equation 9).[54] Therefore, the synergistic action of sulfate radical and non-radical (singlet oxygen) leads to the degradation of toluene.

$$Fe^{2+} + HSO_5^{\bullet-} \rightarrow Fe^{3+} + \cdot OH + SO_4^{\bullet-} \quad \text{(Equation 1)}$$

$$Fe^{3+} + HSO_5^{\bullet-} \rightarrow Fe^{2+} + H^+ + SO_5^{\bullet-} \quad \text{(Equation 2)}$$

$$Co^{2+} + HSO_5^{\cdot-} \rightarrow Co^{3+} + \cdot OH + SO_4^{\bullet-} \quad \text{(Equation 3)}$$

$$Co^{3+} + HSO_5^{\cdot-} \rightarrow Co^{2+} + H^+ + SO_5^{\bullet-} \quad \text{(Equation 4)}$$

$$Mo^{4+} + HSO_5^{\bullet-} \rightarrow Mo^{6+} + \cdot OH + SO_4^{\bullet-} \quad \text{(Equation 5)}$$

$$Mo^{6+} + HSO_5^{\bullet-} \rightarrow Mo^{4+} + H^+ + SO_5^{\bullet-} \quad \text{(Equation 6)}$$

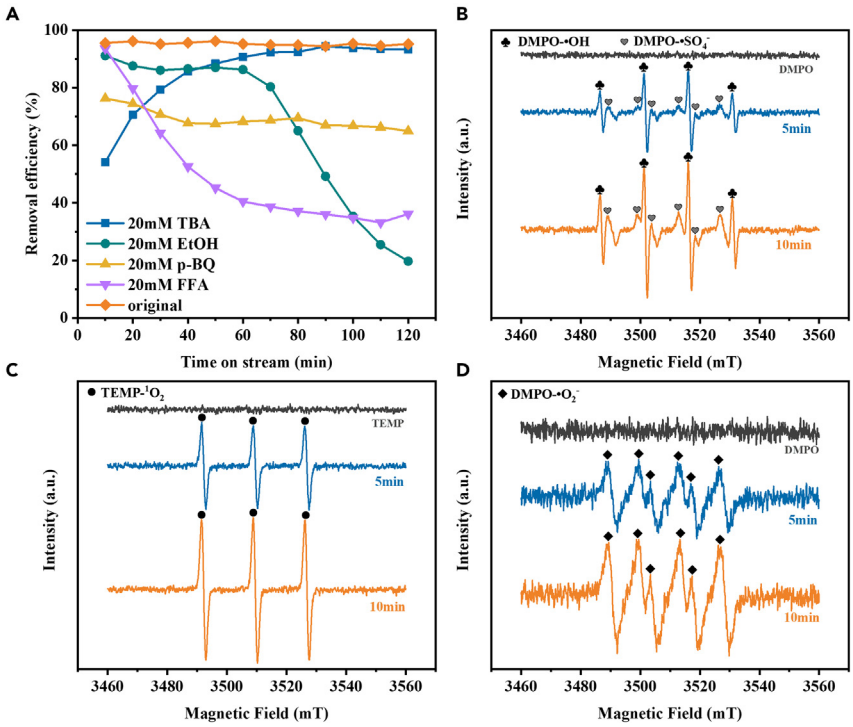

Figure 7. Free radical quenching experiment and EPR spectrum

(A) Effects of radical scavengers on toluene degradation.

(B–D) EPR spectra of PMS activated by CF/MS with time using DMPO and TEMP as trapping reagents.

$$Mo^{6+} + Fe^{3+} \rightarrow Mo^{4+} + Fe^{2+} \quad \text{(Equation 7)}$$

$$2SO_5^{\bullet-} + H_2O \rightarrow 1.5\,{}^1O_2 + 2SO_4^{2-} \quad \text{(Equation 8)}$$

$$O_2^{\bullet-} + \cdot OH \rightarrow {}^1O_2 + OH^- \quad \text{(Equation 9)}$$

$$SO_4^{\bullet-}/\cdot OH/{}^1O_2/O_2^{\bullet-} + \text{Toluene} \rightarrow \text{Intermediate product} \rightarrow CO_2/H_2O, \text{ etc.} \quad \text{(Equation 10)}$$

Active oxygen sites identification

The free radicals involved in the activation of PMS include $SO_4^{\bullet-}/\cdot OH$, O_2^-, and $^1O_2$ mediated electron transfer, namely their roles need to be elucidation in order to better understand the reaction mechanism. The radical quenching experiments were conducted to identify the primary free radicals generated within the CF/MS/PMS system. EtOH and TBA were selected as the quenchers of $SO_4^{\bullet-}$ and $\cdot OH$, and p-BQ and FFA were selected as quenchers of O_2^- and singlet oxygen, respectively. EtOH can eliminate both $\cdot OH$ (1.2–2.8 × 10^9 M^{-1} S^{-1}) and $SO_4^{\bullet-}$ (1.6–7.7 × 10^7 M^{-1} S^{-1}) at the same time. TBA exhibits a higher reaction rate with $\cdot OH$ (3.8–7.6 × 10^8 M^{-1} S^{-1}) than $SO_4^{\bullet-}$ (4.0–9.1 × 10^5 M^{-1} S^{-1}).[55,56] The obtained results revealed that a certain amount of ethanol can inhibit the degradation of toluene, the degradation efficiency decreased from 91% to 20%, verifying the presence of $SO_4^{\bullet-}$ and $\cdot OH$ in the degradation of toluene.

Figure 7A revealed the inhibitory effect of TBA on toluene degradation. It could be inferred that the contribution of $SO_4^{\bullet-}$ radical over that of $\cdot OH$. Introduction of p-BQ yielded an initial toluene efficiency of 76.27% within the first 10 min, which was decreased to 64.95% after 2 h, with a change of 11.32%. Similarly, the presence of FFA precipitated a swift decline in degradation efficiency, plummeting from 93.57% to 36.19%. The inhibitory effect was more obvious than that of TBA, proving a major role of $SO_4^{\bullet-}$ and $^1O_2$ in the degradation process. Furthermore, the active free radicals produced by CF/MS/PMS system were confirmed by using DMPO and TEMP as free radical collector for EPR

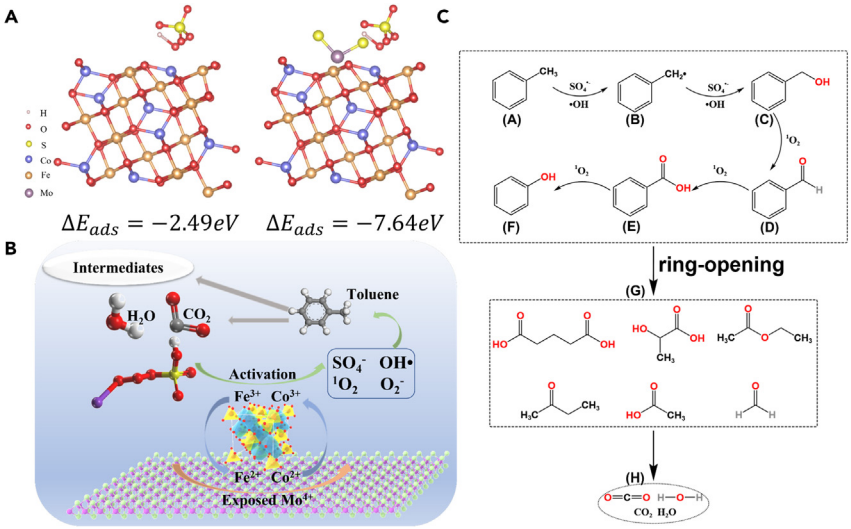

Figure 8. PMS activation mechanism

(A) The adsorption model of PMS on catalyst surface.

(B) Degradation mechanism of toluene.

(C) The degradation pathway of toluene in MS co-catalytic CF/PMS system.

detection. The EPR characterization exhibited clear signals corresponding to DMPO-·OH (1:2:2:1) and DMPO-$SO_4^{\cdot-}$ (1:1:1:1) within the CF/MS/PMS system, and the intensity of DMPO-·OH exceeded that of DMPO-$SO_4^{\cdot-}$.[57,58] The observed outcomes demonstrated that the presence of MoS_2 as a co-catalyst significantly enhances the degree of PMS activation, leading to a substantial generation of free radicals. In addition, weak DMPO $\cdot O_2^-$ signal and obvious TEMP $^1O_2$ characteristic signal were also observed in the system, further affirming the substantial generation of free radicals during toluene degradation within the CF/MS/PMS system. In summary, the catalytic degradation of toluene via the CF/MS/PMS system encompasses both free radical and non-free radical pathways. Among them, $SO_4^{\cdot-}$ and $^1O_2$ emerged as the primary contributor, while the roles of free radicals ·OH and $\cdot O_2^-$ remain limited in the toluene degradation process. Furthermore, As illustrated in Figure S5A, when 2 g/L PMS solution was added in 60 s, a significant negative current peak could be observed on the I-t current curve. Then toluene was injected in 180 s, and obvious current output changes also occurred. This phenomenon suggested that CF/MS as a conductor facilitated the transfer of electrons from toluene to PMS. Furthermore, the corresponding LSV curve in Figure S5B demonstrated a substantial surge in current density upon PMS addition to the electrolyte, signifying electron transfer from CF/MS to PMS. The subsequent addition of toluene further enhanced the current density, indicating that electrons were transferred from the catalyst-PMS complex to toluene.

Toluene degradation pathway

The established models of PMS adsorption on the catalyst's crystal surface depicted the adsorption behavior of PMS (Figure 8A). The adsorption energy of PMS on the CF (311) crystal surface (E_{ads} = −2.49 eV) was notably weaker compared to its adsorption on the MS surface (E_{ads} = −7.64 eV) ($E_{ads} = E_{catalyst + PMS} - E_{PMS} - E_{catalyst}$). It was suggested that Fe^{3+}/Fe^{2+} adsorbed on the surface of MS can effectively enhanced the adsorption of PMS, which was more conducive to PMS activation on the surface of the catalyst. In order to further investigate the degradation pathway of toluene in CF/MS/PMS system, GC-MS analysis was employed to detect intermediate products resulting from toluene oxidation in both gas and liquid phases through a wet washing system. As depicted in Figure 8B, during toluene degradation, the CF/MS/PMS system identified intermediates including ethyl acetate in the tail gas after 2 h reaction, and intermediates in the liquid phase included benzyl alcohol, benzoic acid, benzaldehyde, etc. Fewer intermediates were detected in the gas phase than in the liquid phase. This finding suggested that the majority of intermediates were retained in the liquid phase rather than being released into the atmosphere, thus minimizing the potential for secondary pollution. The radical quenching experiment underscored the predominant roles of $SO_4^{\cdot-}$ and $^1O_2$ in activating PMS for toluene degradation. Specifically, $SO_4^{\cdot-}$ radicals exhibited selective reactivity, preferentially engaging in direct electron transfer reactions with specific functional groups. On the contrary, ·OH radicals underwent non-selective reactions through a series of reactions such as electron transfer, electrophilic/radical addition, hydrogen extraction, etc.[59] More ·OH radicals were required to attack specific functional groups. As evidenced by the substances detected and analyzed by mass spectrometry, toluene was decomposed into small molecular intermediates (butene, acetic acid, ethyl acetate) in the liquid phase. These intermediates were subsequently attacked by free radicals and decomposed into harmless substances such as CO_2 and H_2O.

The potential toluene degradation pathway by CF/MS/PMS system was depicted in Figure 8C. First, $SO_4^{\cdot-}$ attacks toluene molecules by pulling an electron away from the electron-rich methyl group.[59] Then, the methyl group on toluene molecule was exposed to be attacked by ·OH and $SO_4^{\cdot-}$, forming unstable intermediates, which were oxidized to benzyl alcohol (C), benzaldehyde (D), benzoic acid (E) and other

aromatic intermediates under the action of hydroxyl group. Benzoic acid was attacked by $^1O_2$ and produced phenyl through demethylation of toluene, which was oxidized into phenol (F). Finally, the ring-opening reaction generated short-chain compounds (ethyl acetate, formic acid, ethane, formaldehyde, etc.) (G), which are mineralized into CO_2 and H_2O (H).

Conclusions

In conclusion, we have designed and synthesized a distinctive embedded hybrid structure, the $CoFe_2O_4/MoS_2$ magnetic separable composite catalyst. Through the chemical binding with MoS_2, the highly active Mo^{4+} sites have been effectively incorporated onto the catalyst's surface, enhancing the stable cycling of Fe^{3+}/Fe^{2+} and resulting in an efficiently stable toluene degradation performance. The CF/MS/PMS system exhibited an optimal removal efficiency of 97.5% within 2 h, with a CO_2 generation of 205 ppm. The continuous toluene degradation rate remained above 90% over 8 h and retained a high efficiency of 95% even after 4 operational cycles. The mechanism of toluene degradation by liquid-phase catalytic oxidation was elucidated by combining theoretical calculations and experimental investigations. Our finding confirms the predominant roles of $SO_4^{\bullet-}$ and $^1O_2$ in driving the degradation process. This study offers a scientific insight into the deep mineralization of toluene through heterogeneous low temperature catalytic reaction facilitated by MoS_2 co-catalysis $CoFe_2O_4$.

Limitations of the study

While our study has demonstrated the effectiveness of the composite catalyst in the PMS-based wet scrubber for VOCs removal, it is important to acknowledge certain technical limitations. Specifically, we did not explore the removal efficiency under higher airflows in this research. Addressing this issue warrants further investigation in subsequent studies. Additionally, there is a need to develop PMS-based synergistic oxidation techniques to achieve efficient degradation of high-concentration VOCs under low-temperature conditions. These avenues of research hold promise for advancing the field of VOC removal technologies.

STAR★METHODS

Detailed methods are provided in the online version of this paper and include the following:

- KEY RESOURCES TABLE
- RESOURCE AVAILABILITY
  - Lead contact
  - Materials availability
  - Data and code availability
- EXPERIMENTAL MODEL AND SUBJECT DETAILS
- METHOD DETAILS
  - Fabrication of $CoFe_2O_4$ nanosphere
  - Fabrication of $CoFe_2O_4/MoS_2$ catalysts
  - Equipment and procedures
  - Analytical methods
- THE ELECTROCHEMICAL TEST INFORMATION
  - Theoretical calculation methods
- QUANTIFICATION AND STATISTICAL ANALYSIS

SUPPLEMENTAL INFORMATION

Supplemental information can be found online at https://doi.org/10.1016/j.isci.2023.108054.

ACKNOWLEDGMENTS

This work was supported by Shccig-Qinling Program (2021JLM-27), Lanzhou University-Jinchuan Group Chemical Co., Ltd. Chemical Environmental Protection Industry Joint Laboratory ((20)0837), the Fundamental Research Funds for the Central Universities (China), we also thank Chao Li and Yan Liang at Instrument Analysis Center of Xi'an Jiaotong University.

AUTHOR CONTRIBUTIONS

X-a.Z. and W.Z. completed the experiments and data analysis, and wrote the original manuscript, The DFT theoretical calculation was undertaken by X-w. Z.; The revision of the original manuscript was completed by J.L., T.W., Q.F., and H.Z.; C.K. and Z.Y. designed and supervised the study. All authors had full access to the results and accept the decision to submit for publication.

DECLARATION OF INTERESTS

The authors declare that they have no competing interests.

INCLUSION AND DIVERSITY

We support inclusive, diverse, and equitable conduct of research.

Received: July 20, 2023
Revised: September 4, 2023
Accepted: September 22, 2023
Published: September 26, 2023

REFERENCES

1. Yang, C., Miao, G., Pi, Y., Xia, Q., Wu, J., Li, Z., and Xiao, J. (2019). Abatement of various types of VOCs by adsorption/catalytic oxidation: A review. Chem. Eng. J. *370*, 1128–1153. https://doi.org/10.1016/j.cej.2019.03.232.
2. Xie, R., Liu, G., Liu, D., Liang, S., Lei, D., Dong, H., Huang, H., and Leung, D.Y.C. (2019). Wet scrubber coupled with heterogeneous UV/Fenton for enhanced VOCs oxidation over Fe/ZSM-5 catalyst. Chemosphere *227*, 401–408. https://doi.org/10.1016/j.chemosphere.2019.03.160.
3. Zhang, S., You, J., Kennes, C., Cheng, Z., Ye, J., Chen, D., Chen, J., and Wang, L. (2018). Current advances of VOCs degradation by bioelectrochemical systems: A review. Chem. Eng. J. *334*, 2625–2637. https://doi.org/10.1016/j.cej.2017.11.014.
4. Fernandes, A., Makoś, P., and Boczkaj, G. (2018). Treatment of bitumen post oxidative effluents by sulfate radicals based advanced oxidation processes (S-AOPs) under alkaline pH conditions. J. Clean. Prod. *195*, 374–384. https://doi.org/10.1016/j.jclepro.2018.05.207.
5. Park, J.H., Goldstein, A.H., Timkovsky, J., Fares, S., Weber, R., Karlik, J., and Holzinger, R. (2013). Active atmosphere-ecosystem exchange of the vast majority of detected volatile organic compounds. Science *341*, 643–647. https://www.science.org/doi/10.1126/science.1235053.
6. Liu, B., Ji, J., Zhang, B., Huang, W., Gan, Y., Leung, D.Y.C., and Huang, H. (2022). Catalytic ozonation of VOCs at low temperature: A comprehensive review. J. Hazard Mater. *422*, 126847. https://doi.org/10.1016/j.jhazmat.2021.126847.
7. He, C., Cheng, J., Zhang, X., Douthwaite, M., Pattisson, S., and Hao, Z. (2019). Recent advances in the catalytic oxidation of volatile organic compounds: A Review based on pollutant sorts and sources. Chem. Rev. *119*, 4471–4568. https://doi.org/10.1021/acs.chemrev.8b00408.
8. Liang, X., Chen, X., Zhang, J., Shi, T., Sun, X., Fan, L., Wang, L., and Ye, D. (2017). Reactivity-based industrial volatile organic compounds emission inventory and its implications for ozone control strategies in China. Atmos. Environ. X. *162*, 115–126. https://doi.org/10.1016/j.atmosenv.2017.04.036.
9. Gelles, T., Krishnamurthy, A., Adebayo, B., Rownaghi, A., and Rezaei, F. (2020). Abatement of gaseous volatile organic compounds: A material perspective. Catal. Today *350*, 3–18. https://doi.org/10.1016/j.cattod.2019.06.017.
10. Yang, L., Liu, Q., Han, R., Fu, K., Su, Y., Zheng, Y., Wu, X., Song, C., Ji, N., Lu, X., and Ma, D. (2022). Confinement and synergy effect of bimetallic Pt-Mn nanoparticles encapsulated in ZSM-5 zeolite with superior performance for acetone catalytic oxidation. Appl. Catal. B Environ. *309*, 121224. https://doi.org/10.1016/j.apcatb.2022.121224.
11. Li, Y., Wu, S., Wu, J., Hu, Q., and Zhou, C. (2020). Photothermocatalysis for efficient abatement of CO and VOCs. J. Mater. Chem. A *8*, 8171–8194. https://doi.org/10.1039/d0ta00029a.
12. Hu, Q.-y., Wang, C., and Huang, K.-x. (2015). Biofiltration performance and characteristics of high-temperature gaseous benzene, hexane and toluene. Chem. Eng. J. *279*, 689–695. https://doi.org/10.1016/j.cej.2015.05.019.
13. Zhang, Z.Q., Wang, S.B., Wang, R.G., Zhang, W., Wang, P.L., and Su, X.O. (2016). Low-temperature catalysis for VOCs removal in technology and application: A state-of-the-art review. Catal. Today *8*, 270–278. https://doi.org/10.1016/j.cattod.2015.10.040.
14. Rayaroth, M.P., Marchel, M., and Boczkaj, G. (2023). Advanced oxidation processes for the removal of mono and polycyclic aromatic hydrocarbons - a review. Sci. Total Environ. *857*, 159043. https://doi.org/10.1016/j.scitotenv.2022.159043.
15. Wang, L., Luo, D., Hamdaoui, O., Vasseghian, Y., Momotko, M., Boczkaj, G., Kyzas, G.Z., and Wang, C. (2023). Bibliometric analysis and literature review of ultrasound-assisted degradation of organic pollutants. Sci. Total Environ. *876*, 162551. https://doi.org/10.1016/j.scitotenv.2023.162551.
16. Liu, Y., Liu, L., and Wang, Y. (2021). A critical review on removal of gaseous pollutants using sulfate radical-based advanced oxidation technologies. Environ. Sci. Technol. *55*, 9691–9710. https://doi.org/10.1021/acs.est.1c01531.
17. Fernandes, A., Makoś, P., Khan, J.A., and Boczkaj, G. (2019). Pilot scale degradation study of 16 selected volatile organic compounds by hydroxyl and sulfate radical based advanced oxidation processes. J. Clean. Prod. *208*, 54–64. https://doi.org/10.1016/j.jclepro.2018.10.081.
18. Biard, P.-F., Couvert, A., Renner, C., and Levasseur, J.-P. (2009). Assessment and optimisation of VOC mass transfer enhancement by advanced oxidation process in a compact wet scrubber. Chemosphere *77*, 182–187. https://doi.org/10.1016/j.chemosphere.2009.07.050.
19. Lima, V.N., Rodrigues, C.S.D., Borges, R.A.C., and Madeira, L.M. (2018). Gaseous and liquid effluents treatment in bubble column reactors by advanced oxidation processes. Crit. Rev. Environ. Sci. Technol. *48*, 949–996. https://doi.org/10.1080/10643389.2018.1493335.
20. Giannakis, S., Lin, K.-Y.A., and Ghanbari, F. (2021). A review of the recent advances on the treatment of industrial wastewaters by Sulfate Radical-based Advanced Oxidation Processes (SR-AOPs). Chem. Eng. J. *406*, 127083. https://doi.org/10.1080/10643389.2018.1493335.
21. Liu, G., Ji, J., Huang, H., Xie, R., Feng, Q., Shu, Y., Zhan, Y., Fang, R., He, M., Liu, S., et al. (2017). UV/H_2O_2: An efficient aqueous advanced oxidation process for VOCs removal. Chem. Eng. J. *324*, 44–50. https://doi.org/10.1016/j.cej.2017.04.105.
22. Liu, H., Gao, Y., Wang, J., Ma, D., Wang, Y., Gao, B., Yue, Q., and Xu, X. (2021). The application of UV/O_3 process on ciprofloxacin wastewater containing high salinity: Performance and its degradation mechanism. Chemosphere *276*, 130220. https://doi.org/10.1016/j.chemosphere.2021.130220.
23. Xiao, R., He, L., Luo, Z., Spinney, R., Wei, Z., Dionysiou, D.D., and Zhao, F. (2020). An experimental and theoretical study on the degradation of clonidine by hydroxyl and sulfate radicals. Sci. Total Environ. *710*, 136333. https://doi.org/10.1016/j.scitotenv.2019.136333.
24. Ghanbari, F., and Moradi, M. (2017). Application of peroxymonosulfate and its activation methods for degradation of environmental organic pollutants: Review. Chem. Eng. J. *310*, 41–62. https://doi.org/10.1016/j.cej.2016.10.064.
25. Ushani, U., Lu, X., Wang, J., Zhang, Z., Dai, J., Tan, Y., Wang, S., Li, W., Niu, C., Cai, T., et al. (2020). Sulfate radicals-based advanced oxidation technology in various environmental remediation: A state-of-the-art review. Chem. Eng. J. *402*, 126232. https://doi.org/10.1016/j.cej.2020.126232.
26. Li, Y., Wu, X., Li, J., Wang, K., and Zhang, G. (2018). Z-scheme g-C_3N_4@Cs_xWO_3 heterostructure as smart window coating for UV isolating, Vis penetrating, NIR shielding and full spectrum photocatalytic decomposing VOCs. Appl. Catal. B Environ. *229*, 218–226. https://doi.org/10.1016/j.apcatb.2018.02.024.
27. Zhang, J., Hu, Y., Qin, J., Yang, Z., and Fu, M. (2020). TiO_2-UiO-66-NH_2 nanocomposites as efficient photocatalysts for the oxidation of VOCs. Chem. Eng. J. *385*, 123814. https://doi.org/10.1016/j.cej.2019.123814.
28. Roy, D., Neogi, S., and De, S. (2022). Degradative removal of Sulfamethoxazole through visible light driven peroxymonosulfate activation by direct Z-scheme MIL-53(Co/Fe)/MoS_2 heterojunction composite: Role of dual redox mechanism and efficient charge separation. Process Saf. Environ. Protect. *161*, 723–738. https://doi.org/10.1016/j.psep.2022.03.078.
29. Liu, L., Han, C., Ding, G., Yu, M., Li, Y., Liu, S., Xie, Y., and Liu, J. (2022). Oxygen vacancies-enriched Cu/Co bimetallic oxides catalysts for high-efficiency peroxymonosulfate activation to degrade TC: Insight into the increase of Cu^+ triggered by Co doping.

Chem. Eng. J. *450*, 138302. https://doi.org/10.1016/j.cej.2022.138302.

30. Chen, W., He, D., Huang, J., Zhu, K., Lei, L., He, H., and Ai, Y. (2022). One-step synthesis of novel Fe/Fe_3O_4 embedded in N-doped graphite-like carbon nanosheets with the entangled CNTs to activate peroxymonosulfate for bisphenol a degradation. Sep. Purif. Technol. *295*, 121172. https://doi.org/10.1016/j.seppur.2022.121172.
31. Kang, S., and Hwang, J. (2021). $CoMn_2O_4$ embedded hollow activated carbon nanofibers as a novel peroxymonosulfate activator. Chem. Eng. J. *406*, 127158. https://doi.org/10.1016/j.cej.2020.127158.
32. Zhao, C., Meng, L., Chu, H., Wang, J.F., Wang, T., Ma, Y., and Wang, C.C. (2023). Ultrafast degradation of emerging organic pollutants via activation of peroxymonosulfate over Fe_3C/Fe@N-C-x: Singlet oxygen evolution and electron-transfer mechanisms. Appl. Catal. B Environ. *321*, 122034. https://doi.org/10.1016/j.apcatb.2022.122034.
33. Yuan, R., Jiang, M., Gao, S., Wang, Z., Wang, H., Boczkaj, G., Liu, Z., Ma, J., and Li, Z. (2020). 3D mesoporous α-$Co(OH)_2$ nanosheets electrodeposited on nickel foam: A new generation of macroscopic cobalt-based hybrid for peroxymonosulfate activation. Chem. Eng. J. *380*, 122447. https://doi.org/10.1016/j.cej.2019.122447.
34. Li, J., Gou, G., Zhao, H., Liu, C., Li, N., Li, L., Tan, B., and Lai, B. (2022). Efficient peroxymonosulfate activation by $CoFe_2O_4$-CeO_2 composite: Performance and catalytic mechanism. Chem. Eng. J. *435*, 134840. https://doi.org/10.1016/j.cej.2022.134840.
35. Du, M., Yi, Q., Ji, J., Zhu, Q., Duan, H., Xing, M., and Zhang, J. (2020). Sustainable activation of peroxymonosulfate by the Mo(IV) in MoS_2 for the remediation of aromatic organic pollutants. Chin. Chem. Lett. *31*, 2803–2808. https://doi.org/10.1016/j.cclet.2020.08.002.
36. Wang, F., Liu, S.S., Feng, Z., Fu, H., Wang, M., Wang, P., Liu, W., and Wang, C.C. (2022). High-efficient peroxymonosulfate activation for rapid atrazine degradation by FeS_x@MoS_2 derived from MIL-88A(Fe). J. Hazard Mater. *440*, 129723. https://doi.org/10.1016/j.jhazmat.2022.129723.
37. Li, J., Hu, C., Liu, B., and Liu, Z. (2023). Dual pathway reduction of Mo^{4+} and photogenerated electrons restore catalytic sites to enhance heterogeneous peroxymonosulfate activation system. Chem. Eng. J. *452*, 139246. https://doi.org/10.1016/j.cej.2022.139246.
38. Zeng, Y., Guo, N., Song, Y., Zhao, Y., Li, H., Xu, X., Qiu, J., and Yu, H. (2018). Fabrication of Z-scheme magnetic MoS_2/$CoFe_2O_4$ nanocomposites with highly efficient photocatalytic activity. J. Colloid Interface Sci. *514*, 664–674. https://doi.org/10.1016/j.jcis.2017.12.079.
39. Tian, L., Wu, R., and Liu, H. (2019). Synthesis of Au-nanoparticle-loaded 1T@2H-MoS_2 nanosheets with high photocatalytic performance. J. Mater. Sci. *54*, 9656–9665. https://doi.org/10.1007/s10853-019-03545-1.
40. Li, X., Si, Z., Lei, Y., Tang, J., Wang, S., Su, S., Song, S., Zhao, L., and Zhang, H. (2010). Direct hydrothermal synthesis of single-crystalline triangular Fe_3O_4 nanoprisms. CrystEngComm *12*, 2060–2063. https://doi.org/10.1039/b926780h.
41. Cheng, W., Tang, K., Qi, Y., Sheng, J., and Liu, Z. (2010). One-step synthesis of superparamagnetic monodisperse porous Fe_3O_4 hollow and core-shell spheres. J. Mater. Chem. *20*, 1799–1805. https://doi.org/10.1039/b919164j.
42. Togashi, T., Naka, T., Asahina, S., Sato, K., Takami, S., and Adschiri, T. (2011). Surfactant-assisted one-pot synthesis of superparamagnetic magnetite nanoparticle clusters with tunable cluster size and magnetic field sensitivity. Dalton Trans. *40*, 1073–1078. https://doi.org/10.1039/c0dt01280g.
43. Zhou, Y., Liu, Y., Zhang, M., Han, Q., Wang, Y., Sun, X., Zhang, X., Dong, C., Sun, J., Tang, Z., and Jiang, F. (2022). Rationally designed hierarchical N, P co-doped carbon connected 1T/2H-MoS_2 heterostructures with cooperative effect as ultrafast and durable anode materials for efficient sodium storage. Chem. Eng. J. *433*, 133778. https://doi.org/10.1016/j.cej.2021.133778.
44. Lu, J., Zhou, Y., and Zhou, Y. (2021). Efficiently activate peroxymonosulfate by Fe_3O_4@MoS_2 for rapid degradation of sulfonamides. Chem. Eng. J. *422*, 130126. https://doi.org/10.1016/j.cej.2021.130126.
45. Ye, J., Dai, J., Yang, D., Li, C., Yan, Y., and Wang, Y. (2022). Interfacial engineering of vacancy-rich nitrogen-doped Fe_xO_y@MoS_2 Co-catalytic carbonaceous beads mediated non-radicals for fast catalytic oxidation. J. Hazard Mater. *421*, 126715. https://doi.org/10.1016/j.jhazmat.2021.126715.
46. Yan, Q., Lian, C., Huang, K., Liang, L., Yu, H., Yin, P., Zhang, J., and Xing, M. (2021). Constructing an Acidic Microenvironment by MoS_2 in Heterogeneous Fenton Reaction for Pollutant Control. Angew. Chem., Int. Ed. Engl. *60*, 17155–17163. https://doi.org/10.1002/anie.202105736.
47. Gągol, M., Cako, E., Fedorov, K., Soltani, R.D.C., Przyjazny, A., and Boczkaj, G. (2020). Hydrodynamic cavitation based advanced oxidation processes: Studies on specific effects of inorganic acids on the degradation effectiveness of organic pollutants. J. Mol. Liq. *307*, 113002. https://doi.org/10.1016/j.molliq.2020.113002.
48. Rayaroth, M.P., Boczkaj, G., Aubry, O., Aravind, U.K., and Aravindakumar, C.T. (2023). Advanced Oxidation Processes for Degradation of Water Pollutants—Ambivalent Impact of Carbonate Species. A Review, Water *15*, 1615. https://doi.org/10.3390/w15081615.
49. Xu, Y., Ai, J., and Zhang, H. (2016). The mechanism of degradation of bisphenol A using the magnetically separable CuFe2O4/peroxymonosulfate heterogeneous oxidation process. J. Hazard Mater. *309*, 87–96. https://doi.org/10.1016/j.jhazmat.2016.01.023.
50. Rayaroth, M.P., Aravindakumar, C.T., Shah, N.S., and Boczkaj, G. (2022). Advanced oxidation processes (AOPs) based wastewater treatment - unexpected nitration side reactions - a serious environmental issue: A review. Chem. Eng. J. *430*, 133002. https://doi.org/10.1016/j.cej.2021.133002.
51. Chen, Y., Lan, S., and Zhu, M. (2021). Construction of piezoelectric $BaTiO_3$/MoS_2 heterojunction for boosting piezo-activation of peroxymonosulfate. Chin. Chem. Lett. *32*, 2052–2056. https://doi.org/10.1016/j.cclet.2020.11.016.
52. Li, C., Yang, S., Bian, R., Tan, Y., Dong, X., Zhu, N., He, X., Zheng, S., and Sun, Z. (2021). Clinoptilolite mediated activation of peroxymonosulfate through spherical dispersion and oriented array of $NiFe_2O_4$: Upgrading synergy and performance. J. Hazard Mater. *407*, 124736. https://doi.org/10.1016/j.jhazmat.2020.124736.
53. Huang, M., Wang, X., Liu, C., Fang, G., Gao, J., Wang, Y., and Zhou, D. (2021). Mechanism of metal sulfides accelerating Fe(II)/Fe(III) redox cycling to enhance pollutant degradation by persulfate: Metallic active sites vs. reducing sulfur species. J. Hazard Mater. *404*, 124175. https://doi.org/10.1016/j.jhazmat.2020.124175.
54. Hu, J., Zeng, X., Wang, G., Qian, B., Liu, Y., Hu, X., He, B., Zhang, L., and Zhang, X. (2020). Modulating mesoporous Co_3O_4 hollow nanospheres with oxygen vacancies for highly efficient peroxymonosulfate activation. Chem. Eng. J. *400*, 125869. https://doi.org/10.1016/j.cej.2020.125869.
55. Zhou, X., Luo, H., Sheng, B., Chen, X., Wang, Y., Chen, Q., and Zhou, J. (2021). Cu^{2+}/Cu^{+} cycle promoted PMS decomposition with the assistance of Mo for the degradation of organic pollutant. J. Hazard Mater. *411*, 125050. https://doi.org/10.1016/j.jhazmat.2021.125050.
56. Hou, L., Li, X., Yang, Q., Chen, F., Wang, S., Ma, Y., Wu, Y., Zhu, X., Huang, X., and Wang, D. (2019). Heterogeneous activation of peroxymonosulfate using Mn-Fe layered double hydroxide: Performance and mechanism for organic pollutant degradation. Sci. Total Environ. *663*, 453–464. https://doi.org/10.1016/j.scitotenv.2019.01.190.
57. Cashman, M.A., Kirschenbaum, L., Holowachuk, J., and Boving, T.B. (2019). Identification of hydroxyl and sulfate free radicals involved in the reaction of 1,4-dioxane with peroxone activated persulfate oxidant. J. Hazard Mater. *380*, 120875. https://doi.org/10.1016/j.jhazmat.2019.120875.
58. Wu, S., Wu, W., Fan, J., Zhang, L., Zhong, Y., Xu, H., and Mao, Z. (2023). Rapid activation of peroxymonosulfate with iron(III) complex for organic pollutants degradation via a non-radical pathway. Water Res. *233*, 119725. https://doi.org/10.1016/j.watres.2023.119725.
59. Oh, W.-D., Dong, Z., and Lim, T.-T. (2016). Generation of sulfate radical through heterogeneous catalysis for organic contaminants removal: Current development, challenges and prospects. Appl. Catal. B Environ. *194*, 169–201. https://doi.org/10.1016/j.apcatb.2016.04.003.

STAR★METHODS

KEY RESOURCES TABLE

REAGENT or RESOURCE	SOURCE	IDENTIFIER
Chemicals, peptides, and recombinant proteins		
Ammonium molybdate tetrahydrate	Aladdin	CAS 12054-85-2
Thiourea	Aladdin	CAS 62-56-6
Iron nitrate nonahydrate	Aladdin	CAS 7782-61-8
Cobalt nitrate hexahydrate	Macklin	CAS 10026-22-9
Sodium acetate anhydrous	Aladdin	CAS 127-09-3
Dopamine hydrochloride	Aladdin	CAS 62-31-7
p-Benzoqulnone	Aladdin	CAS 106-51-4
Tert-butyl alcohol	Aladdin	CAS 75-65-0
Furfuryl alcohol	Aladdin	CAS 98-00-0
5,5-dimethyl-1-pyrroline	Sigma-Aldrich	CAS 3317-61-1
2,2,6,6-tetramethyl-4-piperidone	Sigma-Aldrich	CAS 2564-83-2
Ethanol	Fuyu (Tianjin)	CAS 64-17-5
Potassium hydrogenperoxomonosulphate	Rhawn	CAS 10058-23-8

RESOURCE AVAILABILITY

Lead contact

Further information and requests for resources should be directed to and will be fulfilled by the lead contact, Prof. Chuncai Kong (kongcc@xjtu.edu.cn).

Materials availability

This work did not generate new unique reagents.

Data and code availability

- All data will be shared upon request to the lead contact.
- This paper does not report original code.
- Any additional analysis information for this work is available by request to the lead contact.

EXPERIMENTAL MODEL AND SUBJECT DETAILS

This work did not involve experimental model and subject.

METHOD DETAILS

Fabrication of $CoFe_2O_4$ nanosphere

Homogeneous nano-spherical cobalt ferrites were synthesized through a one-step solvothermal process followed by high-temperature calcination. Initially, Co $(NO_3)_2 \cdot 6H_2O$ (6 mmol), Fe $(NO_3)_3 \cdot 9H_2O$ (12 mmol) and CH_3COONa (80 mmol) and Dopamine hydrochloride (10 mmol) were completely dissolved in 70 mL of ethylene glycol and the mixture was stirred for 1 h. Subsequently, the homogeneous solution was transferred into a 100 mL Teflon-lined autoclave which was subsequently maintained at 200°C for 12 h. Afterward, the autoclave was allowed to cool naturally to room temperature and the products were washed 3–5 times with ethanol and deionized water alternately until the supernatant turned transparent. The sample was dried for 12 h at 60°C in a vacuum oven. Finally, the dry sample was calcined at 450°C for 3 h to obtain the target $CoFe_2O_4$ nanosphere.

Fabrication of $CoFe_2O_4/MoS_2$ catalysts

Ammonium molybdate and thiourea were dissolved in 30 mL ultra-pure water at a ratio of 1:35 and stirred until completely dissolved. Then 200 mg of cobalt ferrite nanospheres were mixed with the solution for continuous ultrasonic for 1 h and the mixture was transferred to a 50 mL

Teflon-lined autoclave and maintained for 24 h at 200°C. The resulting product was washed several times by ethanol and ultrapure water and dried for 12 h at 60°C. Additionally, the $CoFe_2O_4/MoS_2$ -x (CF/MS-x) with the same process was obtained as reference samples (x = 3: Mo/S = 412/888 mg, x = 6: Mo/S = 206/444 mg, x = 8: Mo/S = 155/333 mg, x = 13: Mo/S = 95/205 mg).

Equipment and procedures

The degradation of VOCs in CF/MS/PMS system was conducted in a continuous-flow system ((illustrated in the experimental equipment flow chart, Scheme S1), comprising toluene gas distribution system, gas-liquid catalyst oxidation part and analysis system. The catalytic oxidation portion consisted of a glass reactor with an effective working volume of 1 L. According to the typical VOCs emission concentration of the printing coating industry, the inlet gas introduced 30 ppm initial concentration of toluene standard gas along with nitrogen as the carrier gas. Mass flowmeter is used to control gas flow rate to 200 mL/min. The inlet gas was delivered into the reactor via a bottom-mounted bubbler. Ultra-pure water is used in the reaction process, accompanied by magnetic agitation to ensure effective contact between catalyst and PMS. The reaction temperature was maintained at a constant 30°C by the control of the water bath. The catalyst and PMS powder are added to the solution and the reactor is sealed was sealed prior to commencing the degradation experiment. Toluene standard gas was bubbled into the reactor to initiate the catalytic degradation process.

The whole system is in a closed state after initiating the catalytic reaction. We connected the degraded outgassing tube directly to the GC for toluene concentration change and CO_2 concentration detection, while we collected the tail gas and liquid to detect the intermediate products formed by GC-MS for further analysis. Therefore, the degradation efficiency and the amount of CO_2 as well as the mass spectrometry analysis can confirm whether toluene is absorbed or not. Moreover, it has been shown that the degradation of VOCs on the surface of the catalyst has little effect on the overall degradation of VOCs, and thus the degradation of VOCs is highly dependent on the bulk solution. In this case, the role of the catalyst is to effectively activate the oxidant through chemical reactions on its surface, generating free radicals and further reacting with the pollutants in the bulk solution.

It is worth noting that the toluene gas used in the experiment is a standard gas, rather than through the evaporation of toluene solution (there is a large concentration error). The standard gas with equal volume and different concentration is usually calibrated by manual sampling. However, due to the particularity of the experiment, according to the suggestion of gas chromatography engineer, in order to further reduce the error, we adopted mobile phase toluene standard gas automatic injection for calibration. The external standard method was employed for the calibration of the gas chromatograph using standard toluene gas (1 ppm, 30 ppm, 100 ppm). The standard toluene gas was automatically injected into the system in 5 groups, and the peak heights of the standard samples overlapped, with a retention time of 3.5 min.

Curve equation: $Y = 1.02002X-0.31727$; $R^2 = 0.9999849$.

Analytical methods

The size and morphologies of catalysts were observed by transmission electron microscopy (TEM, Talos L120C G2/Talos F200X) and scanning electron microscope (SEM, ThermoFisher Apreo S)). The crystal structure of the samples was examined by X-ray diffraction (XRD, Bruker D8 ADVANC). X-ray diffractometer with Ni-filtered Cu Kα radiation in 2θ ranging from 5° to 80°. The elemental and valence analysis were characterized by X-ray photoelectron spectroscopy (XPS, Thermo Fisher Scientific ESCALAB Xi+ spectrometer). The structure of the samples was determined by FTIR spectrometer (Thermo Fisher Scientific Nicolet iS50). A gas chromatograph (GC) (GC-7920, Beijing China Education Au-light Co., Ltd.) equipped with two flame-ionization detectors (FID) was measured the inlet and outlet concentrations of toluene and CO_2 (FID1 was used to detect toluene, and FID2 was equipped with a methanizer that converts CO_2 to CH_4 for detection.) The gas samples are collected online through an automatic sampling valve for detection (Toluene, SE-54 column, 30 m × 0.32 mm ×0.5 μm; CO_2, TDX-01 column, 1 m × 3 mm). The stationary phase of TDX-01 column was carbon molecular sieve. Using DMPO and TEMP as spin trapping reagent, the presence of free radicals was determined by EPR test at room temperature. Total organic carbon analyzer is used to test total organic carbon (TOC). The Gas Chromatography-Mass Spectrometer (Triple quadrupole GC-MS, Agilent 8890-7000D) was used to detect intermediates extracted using dichloromethane in the water and gas phases.

THE ELECTROCHEMICAL TEST INFORMATION

The electrochemical experiments were conducted on electrochemical workstation (CHI660e, CH Instruments, China) with standard three-electrode system. Wherein, 2 mg catalyst, 336 μL Isopropyl alcohol, 144 μL deionized water and 20 μL Nafion solution (5%) were mixed with ultrasonic for 30 min until forming uniform slurry. Next, 10μL uniform slurry was dropped onto the glassy carbon electrode and dried naturally at room temperature to form working electrode. The electrolyte was 50 mM Na_2SO_4 solution, platinum plate was used as the counter electrode and the reference electrode was Ag/AgCl electrode. The electrochemical data about i-t curves and linear sweep voltammetry (LSV) were obtained from workstation.

Theoretical calculation methods

Using the density functional principle (DFT) and Cambridge Sequential Total Energy Package (CASTEP) module in Materials studio software, a slab model is established on the (311) crystal plane with $CoFe_2O_4$ anti-spinel structure. The 12-layer atomic thickness is selected to build a 15 mm vacuum layer along the z axis direction. Perdew-Burke-Ernzerhof (PBE) of the generalized gradient integral (GGA) is adopted as

the function. Compared with the ultra-soft pseudopotential, the ultrasoft pseudopotential optimized by OTFG can obtain more accurate results. The cutoff energy of electron plane wave is set to 500 eV and K-Piont in Brillouin zone is set to 1 × 2×1. The convergence criteria of energy, maximum stress, maximum interatomic displacement and maximum interatomic force are 10^{-5} eV, 0.05 G Pa, 0.001 Å and 0.03 eV/Å, respectively.

QUANTIFICATION AND STATISTICAL ANALYSIS

No statistical analysis is used.